Supporting Information: Consistent Device Simulation Model Describing Perovskite Solar Cells in Steady-State, Transient and Frequency Domain

Martin T. Neukom[a,b,c], Andreas Schiller[a,b,*], Simon Züfle[a,b], Evelyne Knapp[a], Jorge Ávila[d], Daniel Pérez-del-Rey[d], Chris Dreessen[d], Kassio Zanoni[d], Michele Sessolo[d], Henk J. Bolink[d] and Beat Ruhstaller[a,b]

[a] Institute of Computational Physics, Zurich University of Applied Sciences, Wildbachstr. 21, 8401 Winterthur, Switzerland
[b] Fluxim AG, Loft 313, Katharina-Sulzer-Platz 2, 8400 Winterthur, Switzerland
[c] Institute of Physics, University of Augsburg, 86135 Augsburg, Germany
[d] Instituto de Ciencia Molecular, Universidad de Valencia, C/J. Beltrán 2, 46980 Paterna, Spain

* Corresponding Author: andreas.schiller@fluxim.com

1. Physical Model

1.1. Model Equations

In this section the governing equations of the drift-diffusion model implemented in Setfos 4.6 [1] are explained. The quantities are described in the next section.

1.1.1. Electronic Drift-Diffusion
The continuity equations for electrons and holes govern the change in charge carrier density due to current flow, electron or hole exchange with traps, recombination and generation.

$$\frac{\partial n_e}{\partial t}(x,t) = \frac{1}{q} \cdot \frac{\partial j_e}{\partial x}(x,t) - R_{te}(x,t) - R(x,t) + G_{opt} \cdot g(x) \qquad \text{Eq. 1a}$$

$$\frac{\partial n_h}{\partial t}(x,t) = -\frac{1}{q} \cdot \frac{\partial j_h}{\partial x}(x,t) - R_{th}(x,t) - R(x,t) + G_{opt} \cdot g(x) \qquad \text{Eq. 1b}$$

For the calculation of the charge generation profile g(x) Setfos considers the measured illumination spectrum, the complex refractive indices and the thickness of each layer of the cell stack.

Radiative recombination is described by

$$R(x,t) = \beta \cdot n_e(x,t) \cdot n_h(x,t) \qquad \text{Eq. 2}$$

The currents of electrons and holes consist of drift in the electric field and diffusion due to the charge carrier density gradients. Hereby the absolute unit charge q=1.6·10⁻¹⁹C and the sign convention for the current according to Selberherr [2] are used.

$$j_e(x,t) = n_e(x,t) \cdot q \cdot \mu_e \cdot E(x,t) + \mu_e \cdot k_B \cdot T \cdot \frac{\partial n_e}{\partial x}(x,t) \qquad \text{Eq. 3a}$$

$$j_h(x,t) = n_h(x,t) \cdot q \cdot \mu_h \cdot E(x,t) - \mu_h \cdot k_B \cdot T \cdot \frac{\partial n_h}{\partial x}(x,t) \qquad \text{Eq. 3b}$$

1.1.2. Ionic Drift-Diffusion
The continuity equation for anions and cations governs the change in ion density due to ionic current flow.

$$\frac{\partial n_a}{\partial t}(x,t) = \frac{1}{q} \cdot \frac{\partial j_a}{\partial x}(x,t) \qquad \text{Eq. 4a}$$

$$\frac{\partial n_c}{\partial t}(x,t) = -\frac{1}{q} \cdot \frac{\partial j_c}{\partial x}(x,t) \qquad \text{Eq. 4b}$$

Ions diffuse due to a density gradient or drift in the electric field.

$$j_a(x,t) = n_a(x,t) \cdot q \cdot \mu_a \cdot E(x,t) + \mu_a \cdot k_B \cdot T \cdot \frac{\partial n_a}{\partial x}(x,t) \qquad \text{Eq. 5a}$$

$$j_c(x,t) = n_c(x,t) \cdot q \cdot \mu_c \cdot E(x,t) - \mu_c \cdot k_B \cdot T \cdot \frac{\partial n_c}{\partial x}(x,t) \qquad \text{Eq. 5b}$$

The continuity and drift-diffusion equations for negatively/positively charged ions are thus equivalent to the ones for electrons and holes, except that the ions cannot leave the perovskite layer and generation/recombination is excluded.

1.1.3. Total Current, Poisson and Device Voltage

The total current is the sum of electron current, hole current, anion current, cation current, displacement current and the current through the parallel resistance. This total current is constant in x.

$$j(x,t) = j_e(x,t) + j_h(x,t) + j_a(x,t) + j_c(x,t) + \frac{\partial E}{\partial t}(x,t) \cdot \varepsilon + \frac{V_{dev}(t)}{R_p}$$

Eq. 6

The Poisson equation relates the electric field with the charges inside the layer.

$$\frac{\partial E}{\partial x}(x,t) = -\frac{q}{\varepsilon} \cdot [n_h(x,t) - n_e(x,t) + n_c(x,t) - n_a(x,t)$$
$$+ n_{t,h}(x,t) - n_{t,e}(x,t) + n_{p-doping}(x) - n_{n-doping}(x)]$$

Eq. 7

The integral of the electric field over position x plus the built-in voltage is called device voltage. It is the applied voltage minus the voltage drop over the series resistance [3].

$$V_{dev}(t) = \int_0^d E(x,t) \cdot dx + V_{bi} = V_{applied}(t) - R_S \cdot j(t) \cdot S$$

Eq. 8

1.1.4. The Built-In Voltage

The built-in voltage is defined as the difference in workfunctions of the electrodes. The workfunctions are calculated using the boundary charge carrier densities n_{h0} and n_{e0}.

$$V_{bi} = \frac{\phi_A - \phi_C}{q}$$

Eq. 9

$$\phi_C = E_{LUMO} - \ln\left(\frac{n_{e0}}{N_0}\right) \cdot k_B \cdot T$$

Eq. 10a

$$\phi_A = E_{HOMO} + \ln\left(\frac{n_{h0}}{N_0}\right) \cdot k_B \cdot T$$

Eq. 10b

1.1.5. Boundary Conditions

As boundary conditions the electron density at the anode and the hole density at the cathode are set to fixed values n_{e0} and n_{h0}.

$$n_h(0,t) = n_{h0}$$

Eq. 11a

$$n_e(0,t) = N_0^2 \cdot \exp\left(-\frac{E_g}{k_B \cdot T}\right) \cdot \frac{1}{n_{h0}}$$

Eq. 11b

$$n_e(d,t) = n_{e0}$$

Eq. 11c

$$n_h(d,t) = N_0^2 \cdot \exp\left(-\frac{E_g}{k_B \cdot T}\right) \cdot \frac{1}{n_{e0}}$$

Eq. 11d

The electric potential is evaluated according to

$$\varphi(x,t) = \int_0^x E(x',t) \cdot dx'$$

Eq. 12a

$$\varphi(0,t) = 0$$

Eq. 12b

$$\varphi(d,t) = V_{dev}(t) - V_{bi}(t)$$

Eq. 12c

As ions cannot leave the perovskite layer the ionic current is set to zero at the interface HTM-MAPI (position d_1) and at the interface MAPI-ETM (position d_2).

$$j_a(d_1, t) = 0 \qquad\qquad \text{Eq. 13a}$$

$$j_c(d_1, t) = 0 \qquad\qquad \text{Eq. 13b}$$

$$j_a(d_2, t) = 0 \qquad\qquad \text{Eq. 13c}$$

$$j_c(d_2, t) = 0 \qquad\qquad \text{Eq. 13d}$$

The total ion density is the integral over the perovskite layer.

$$N_a = \frac{1}{d} \cdot \int_0^d n_a(x, t) \cdot dx \qquad\qquad \text{Eq. 14a}$$

$$N_c = \frac{1}{d} \cdot \int_0^d n_c(x, t) \cdot dx \qquad\qquad \text{Eq. 14b}$$

1.1.6. Trapping

Trapping and de-trapping of electron traps is described by the electron trap continuity equation. The electron trap can either exchange electrons with the LUMO level at the rate R_{te} or exchange holes with the HOMO level at the rate R_{th}.

$$\frac{\partial n_t}{\partial t} = R_{te} - R_{th} \qquad\qquad \text{Eq. 15}$$

Free electrons in the LUMO can be captured by traps. Trapped electrons can be released thermally activated into the LUMO.

$$R_{te} = c_e \cdot n_e \cdot (N_t - n_t) - c_e \cdot N_0 \cdot \exp\left(\frac{E_t - E_{LUMO}}{k_B \cdot T}\right) \cdot n_t \qquad\qquad \text{Eq. 16}$$

Trapped electrons can recombine with a free hole. An empty trap can capture an electron from the HOMO level by thermal activation (leaving behind a hole).

$$R_{th} = c_h \cdot n_h \cdot n_t - c_h \cdot N_0 \cdot \exp\left(-\frac{E_t - E_{HOMO}}{k_B \cdot T}\right) \cdot (N_t - n_t) \qquad\qquad \text{Eq. 17}$$

The three equations above describe SRH-recombination in a two-step process. Free electrons are captured in the trap and subsequently recombine with a free hole. Alternatively, an electron can be thermally activated from the HOMO to the trap level and from the trap level to the LUMO. The latter two routes occur however with lower probability.

1.2. Physical Quantities

Quantity	Quantity	Unit
n_e	Electron density	cm^{-3}
n_h	Hole density	cm^{-3}
n_c	Cation density	cm^{-3}
n_a	Anion density	cm^{-3}
$n_{t,e}$	Density of trapped electrons	cm^{-3}
$n_{t,h}$	Density of trapped holes	cm^{-3}
$n_{n\text{-doping}}$	n-type doping density	cm^{-3}
$n_{p\text{-doping}}$	p-type doping density	cm^{-3}
j_e	Electron current	mA/cm^2
j_h	Hole current	mA/cm^2
j_c	Cation current	mA/cm^2
j_a	Anion current	mA/cm^2
j	Total current	mA/cm^2
E	Electric field	V/m
φ	Electric potential	V
R	Recombination rate	$s^{-1}\ cm^{-3}$
R_{te}	Electron trap – electron exchange rate	$s^{-1}\ cm^{-3}$
R_{th}	Electron trap – hole exchange rate	$s^{-1}\ cm^{-3}$
$g(x)$	Charge generation profile	$s^{-1}\ cm^{-3}$
x	Dimension in layer direction	nm
t	Time	s
d	Full simulation domain width	nm
d1	Position of the interface HTM-MAPI	nm
d2	Position of the interface MAPI-ETM	nm
S	Device area	cm^2
μ_e	Electron mobility	cm^2/Vs
μ_h	Hole mobility	cm^2/Vs
μ_c	Cation mobility	cm^2/Vs
μ_a	Anion mobility	cm^2/Vs
β	Recombination coefficient	cm^3/s
V_{source}	Voltage of the voltage source that is connected to the device	V
V_{bi}	Built-in voltage	V
R_s	Series resistance	Ω
R_p	Parallel resistance	Ω
Φ_A	Workfunction of the anode	eV
Φ_C	Workfunction of the cathode	eV
E_{HOMO}	Energy of highest occupied molecular orbital	eV
E_{LUMO}	Energy of lowest unoccupied molecular orbital	eV
E_t	Trap energy	eV
n_{e0}	Electron density at the right electrode (x=d) as boundary condition of the simulation.	cm^{-3}
n_{h0}	Hole density at the left electrode (x=0) as boundary condition of the simulation.	cm^{-3}
N_0	Density of chargeable sites	cm^{-3}
N_t	Trap density	cm^{-3}
N_c	Total cation density	cm^{-2}
N_a	Total anion density	cm^{-2}
c_e	Capture rate for electrons	cm^3/s
c_h	Capture rate for holes	cm^3/s
G_{opt}	Photon-to-charge conversion efficiency	1

	This factor accounts for non-dissociated excitons.	
ε	Electrical permittivity ($\varepsilon = \varepsilon_0 \cdot \varepsilon_r$)	F/m
q	Unit charge	C
k_B	Boltzmann constant	J/K
T	Temperature	K

Table S1: *Physical quantities used in the equations of the previous section and in the main text.*

2. Model Parameter Analysis

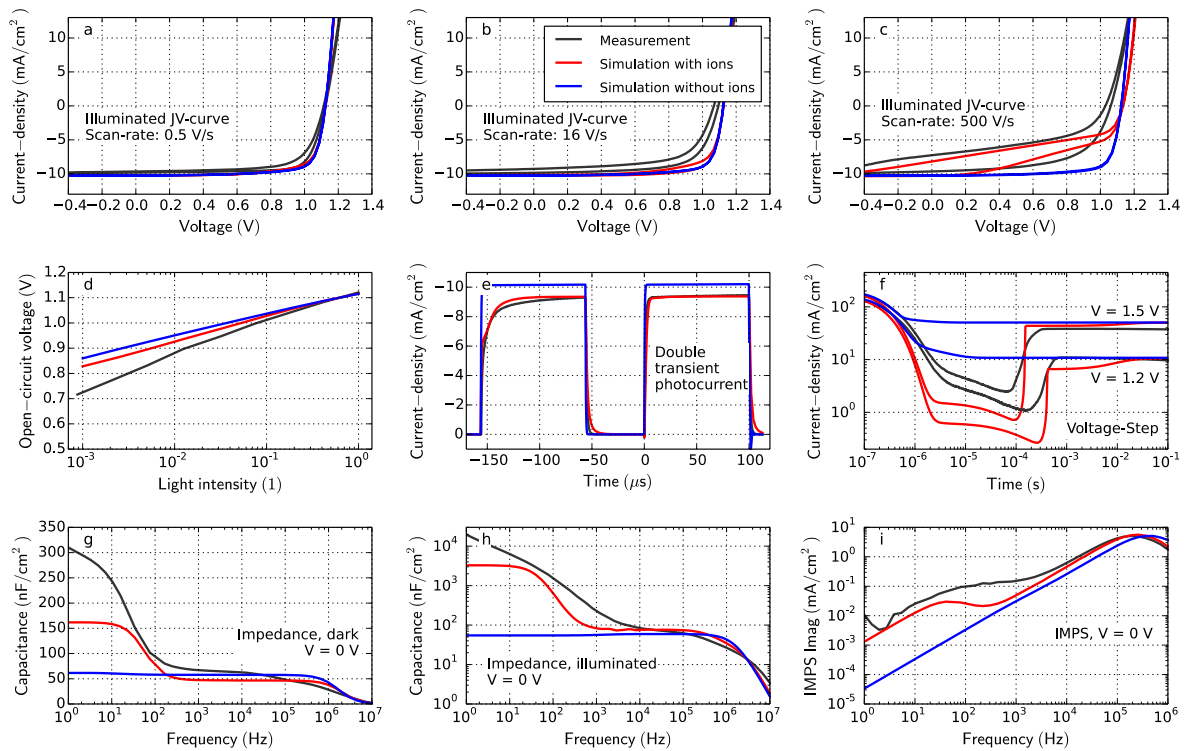## 2.1. Simulation Results with and without Mobile Ions

Figure S1: Comparison of simulation with (red) and without (blue) mobile ions. The measurement is shown in black. (a-i) The figure type is identical to Figure 3 a-i in the manuscript.

Figure S1 shows the comparison of the simulation result with and without mobile ions. From Figure S1c it is evident that the JV-curve hysteresis only occurs in the presence of mobile ions in our model.

The slow current-rise observed in the double light pulse (Figure S1e) caused by slow trapping disappears without mobile ions. The mobile ions do not move on these time-scales, but their accumulation at the interface in steady-state lowers the effective field in the device. In the case without the mobile ions the trap-filling is still a slow process, but the current can rise fast enough due to the high built-in field. The characteristic current-rise in Figure S1f disappears without mobile ions. Charges can be injected from the very beginning of the voltage step.

The low frequency effects in impedance spectroscopy (Figure S1g and Figure S1h) disappear when ions are disabled. The same is true for the low frequency shoulder in IMPS in Figure S1i.

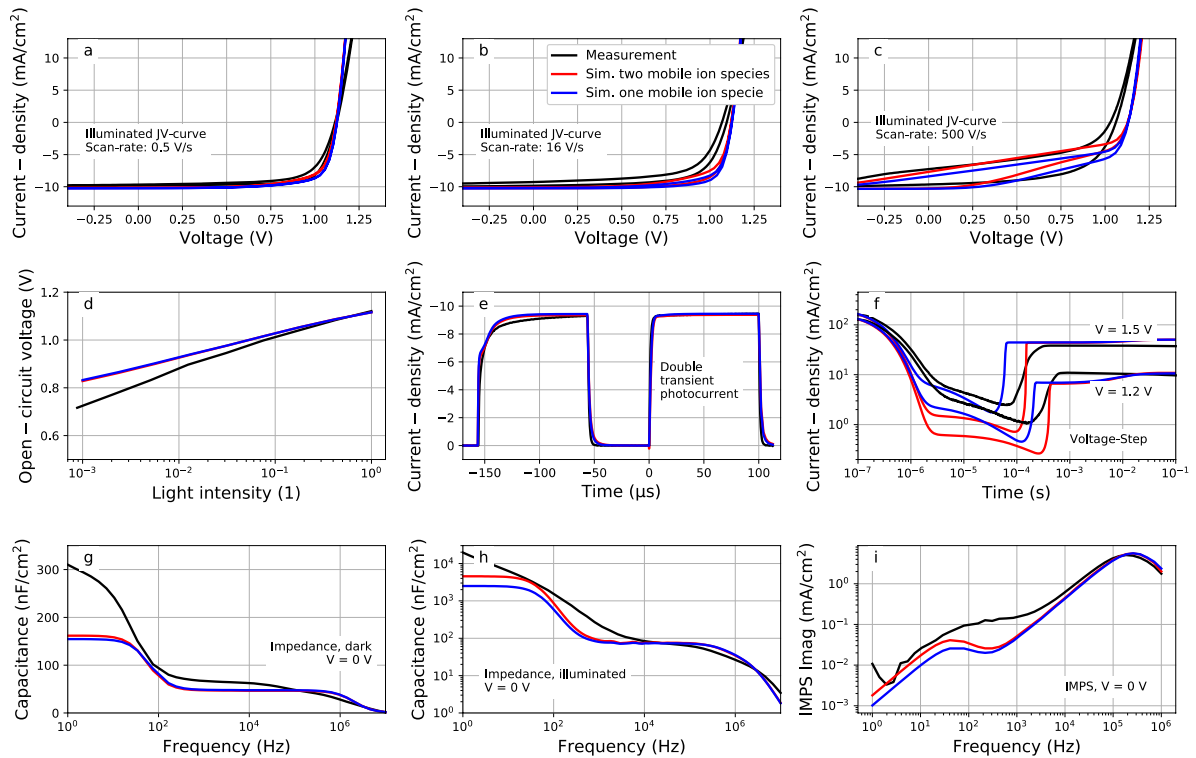## 2.2.   Simulation Results with one Mobile Ionic Specie

Figure S2: Comparison of simulation with two mobile ionic species (red) and with one mobile ionic species (blue). The measurement is shown in black. (a-i) The figure type is identical to Figure 3 a-i in the manuscript.

There are several ionic species moving inside a methylammonium perovskite solar cell. There is convincing evidence, that iodine vacancies (positively charged) are mobile [4–6]. There is evidence that methylammonium vacancies (negatively charged) are mobile too but have a much lower mobility [6–8]. Numerical simulations with mobile ions have been performed with one species mobile and one species immobile [9–11] as well as with two mobile species [12–14]. Figure S2 shows a comparison between those two simulations. The red curve is the same as in the manuscript using two mobile species. The blue line is the simulation result using one mobile type (positively charged iodine vacancies). In this case the negatively charged MA vacancies of the same density are modelled as homogeneously distributed fixed space charge (doping).
Interestingly, the results of the two simulations look almost identical. Apart from the rise-time in the transient voltage step experiment (Figure S2f), all major effects are also observed if only one ion type is mobile.
We conclude that, as long as the mobility of the MA ions is very low, it is not of great importance to the simulation result whether one or two mobile ionic species are considered.

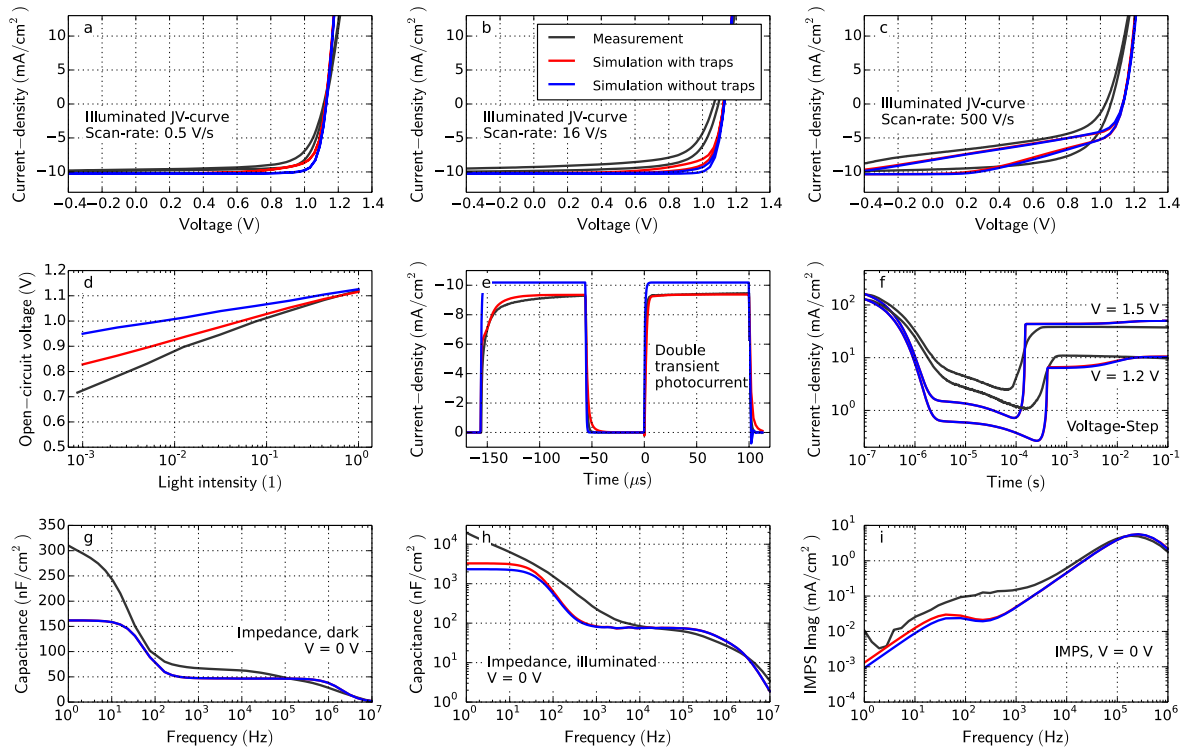## 2.3. Simulation Results with and without Traps

*Figure S3: Comparison of simulation with trapping (red) and without trapping (blue). The measurement
is shown in black. (a-i) The figure type is identical to Figure 3 a-i in the manuscript.*

Figure S3 shows the comparison between simulation with traps and Shockley-Read-Hall
(SRH) recombination and without traps.
Without traps and without SRH-recombination the fill factor is increased (Figure S3a), the
ideality factor is close to 1.0 (Figure S3d). Without SRH-recombination the measurement
results cannot be reproduced.
If trapping is disabled in the simulation the current-rise in the double light pulse experiment
(Figure S3e) is faster. Both the first and the second response look identical. All other
experiments in Figure S3 are only marginally influenced by trapping and SRH-recombination.

3. Voltage Pulse – Influence of Surface Recombination

The shape of the current-rise as response to a voltage step depends critically on the surface recombination. Figure S4a shows the simulation result of the perovskite solar cell of the manuscript (blue line). In this case the surface recombination is very low. The green line shows the simulation result with a high surface recombination. The rise-time is significantly slower compared to the case with passivated surfaces.
Surface recombination is modelled by a thin layer close to the interface where the recombination pre-factor is much larger than in the bulk.

To further investigate this effect, we fabricated devices with and without a 10 nm thick intrinsic passivation layer between perovskite and the doped ETL and HTL, respectively. These extra layers are expected to supress surface recombination [15]. Voltage-step measurements on devices with and without these passivation layers are shown in Figure S4b. The current rise of the device without passivation layers is much slower. This behaviour is consistent with the simulation with a high surface recombination.

We conclude that a steep current-rise in the voltage step experiment is an indicator for well passivated surfaces.
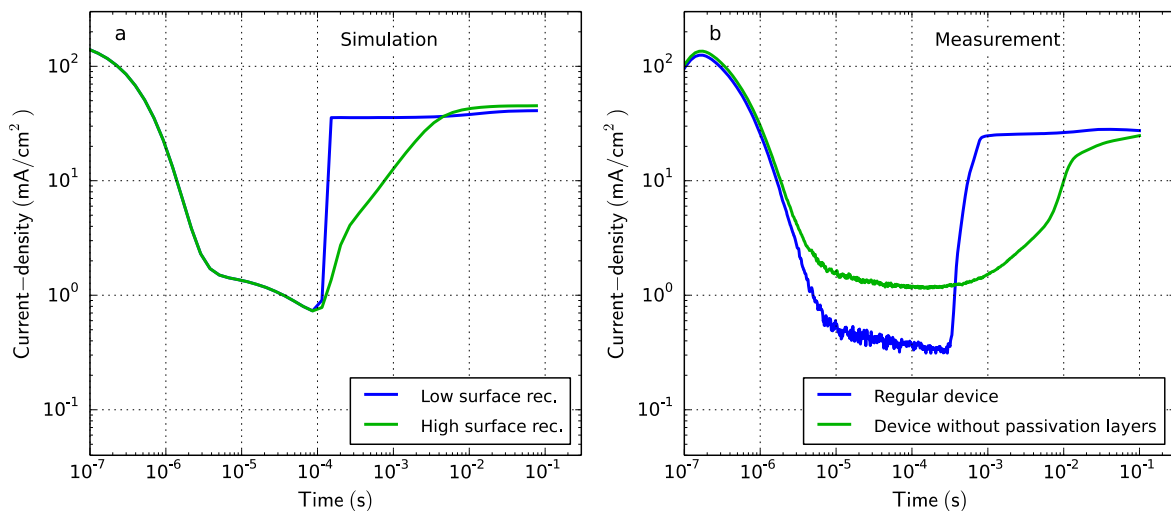

Figure S4: Transient current as response to a voltage step. a) Numerical simulation with varied surface recombination. b) Measurement of two different MAPI perovskite solar cells.

4. JV-Curve Hysteresis

Even in the presence of mobile ions a perovskite solar cell can be hysteresis-free [11]. In our previous publication we showed that a sufficiently high charge carrier lifetime in combination with a low surface recombination is required for a minimal hysteresis [16].

The device under investigation has a good surface quality (low surface recombination) but a low bulk quality (low charge carrier lifetime). The simulated JV-curve with hysteresis is shown in Figure S5b.
In Figure S5a a device with low bulk quality and lower surface quality is shown. Here the hysteresis is the largest. Figure S5c shows a device with a high bulk quality but a low surface quality. A pronounced hysteresis is observed. Only in the case with high bulk and surface quality the hysteresis is minimal as shown in Figure S5d.

If the surface recombination is low (high surface quality) and the charge carrier lifetime is high (high bulk quality) then charges can be extracted even against the electric field created by the mobile ions [16].
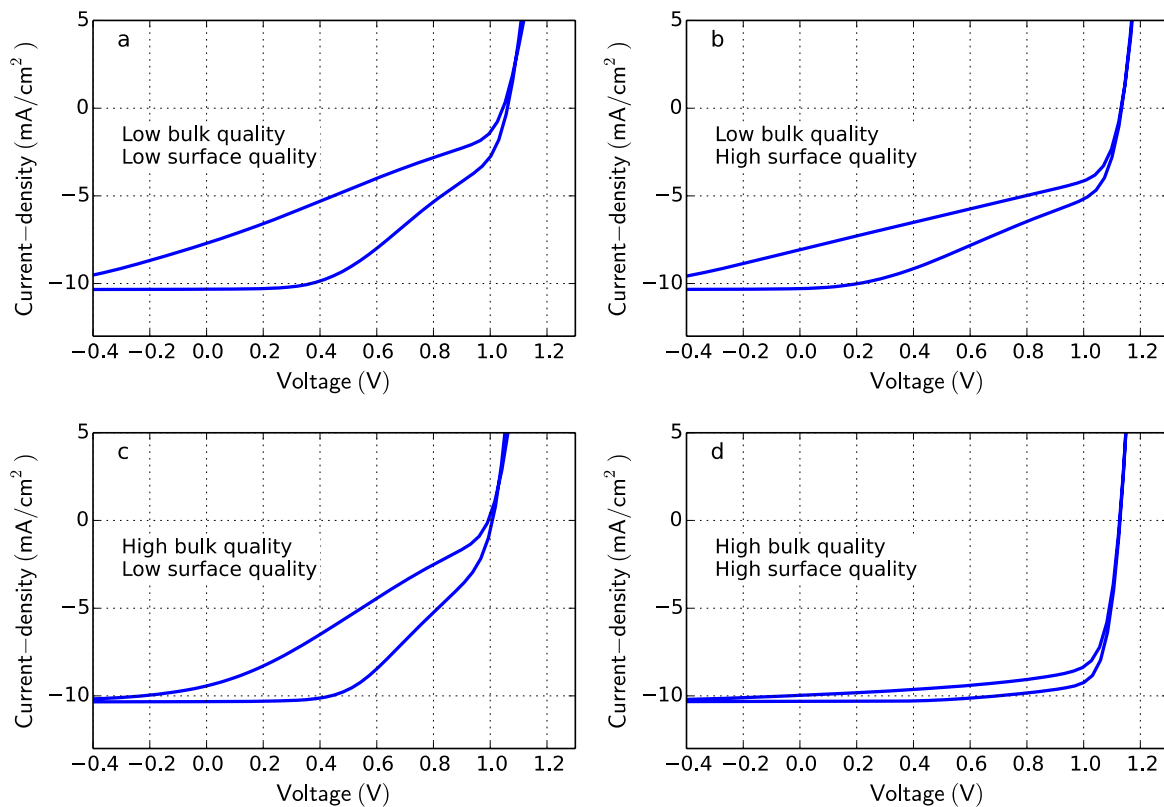

Figure S5: Simulations of JV-curves with hysteresis for different combinations of low (a,b) and high (c,d) bulk qualities and low (a,c) and high (b,d) surface qualities. A ramp-rate of 16 V/s has been used.
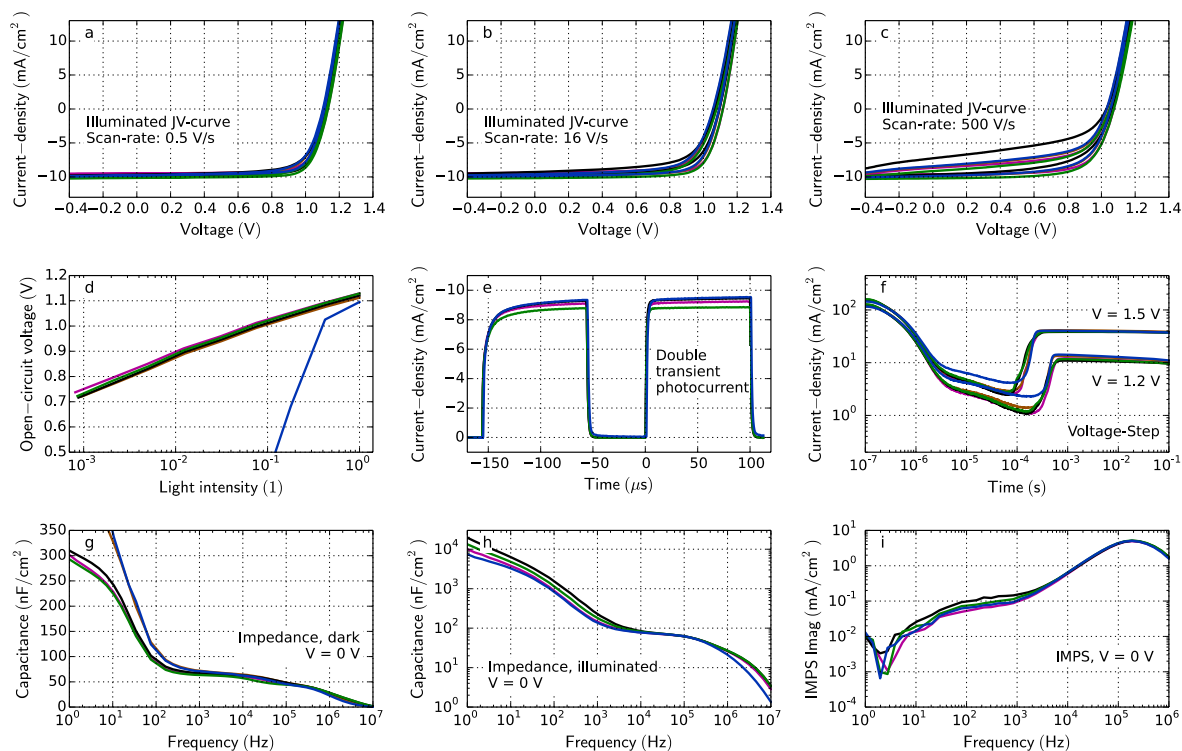
5. All Measurement Data

Figure S6: Measurements of 5 nominally identical devices. (a-i) The figure type is identical to Figure 3 a-i in the manuscript.

Figure S6 shows the measurement data of 5 nominally identical devices. In total 8 devices were measured. Three devices did not work reliably therefore only 5 devices are shown here. The reproducibility of the devices is very good.

6. References

(1) Semiconducting Thin Film Optics Simulator (SETFOS) by Fluxim AG, Switzerland.

(2) S. Selberherr. *Analysis and Simulation of Semiconductor Devices*; Springer: Vienna, 1984.

(3) Neukom, M. T. Charge Carrier Dynamics of Methylammonium Lead-Iodide Perovskite Solar Cells. *ArXiv161106425 Cond-Mat* **2016**.

(4) Lee, H.; Gaiaschi, S.; Chapon, P.; Marronnier, A.; Lee, H.; Vanel, J.-C.; Tondelier, D.; Bourée, J.-E.; Bonnassieux, Y.; Geffroy, B. Direct Experimental Evidence of Halide Ionic Migration under Bias in $CH_3NH_3PbI_{3-x}Cl_x$ -Based Perovskite Solar Cells Using GD-OES Analysis. *ACS Energy Lett.* **2017**, *2* (4), 943–949. https://doi.org/10.1021/acsenergylett.7b00150.

(5) deQuilettes, D. W.; Zhang, W.; Burlakov, V. M.; Graham, D. J.; Leijtens, T.; Osherov, A.; Bulović, V.; Snaith, H. J.; Ginger, D. S.; Stranks, S. D. Photo-Induced Halide Redistribution in Organic–Inorganic Perovskite Films. *Nat. Commun.* **2016**, *7*, 11683. https://doi.org/10.1038/ncomms11683.

(6) Eames, C.; Frost, J. M.; Barnes, P. R. F.; O'Regan, B. C.; Walsh, A.; Islam, M. S. Ionic Transport in Hybrid Lead Iodide Perovskite Solar Cells. *Nat. Commun.* **2015**, *6*, 7497. https://doi.org/10.1038/ncomms8497.

(7) Frost, J. M.; Walsh, A. What Is Moving in Hybrid Halide Perovskite Solar Cells? *Acc. Chem. Res.* **2016**, *49* (3), 528–535. https://doi.org/10.1021/acs.accounts.5b00431.

(8) Walsh, A.; Scanlon, D. O.; Chen, S.; Gong, X. G.; Wei, S.-H. Self-Regulation Mechanism for Charged Point Defects in Hybrid Halide Perovskites. *Angew. Chem. Int. Ed.* **2015**, *54* (6), 1791–1794. https://doi.org/10.1002/anie.201409740.

(9) Richardson, G.; O'Kane, S. E. J.; Niemann, R. G.; Peltola, T. A.; Foster, J. M.; Cameron, P. J.; Walker, A. B. Can Slow-Moving Ions Explain Hysteresis in the Current–Voltage Curves of Perovskite Solar Cells? *Energy Environ. Sci.* **2016**, *9* (4), 1476–1485. https://doi.org/10.1039/C5EE02740C.

(10) O'Kane, S. E. J.; Richardson, G.; Pockett, A.; Niemann, R. G.; Cave, J. M.; Sakai, N.; Eperon, G. E.; Snaith, H. J.; Foster, J. M.; Cameron, P. J.; et al. Measurement and Modelling of Dark Current Decay Transients in Perovskite Solar Cells. *J. Mater. Chem. C* **2017**, *5* (2), 452–462. https://doi.org/10.1039/C6TC04964H.

(11) Calado, P.; Telford, A. M.; Bryant, D.; Li, X.; Nelson, J.; O'Regan, B. C.; Barnes, P. R. F. Evidence for Ion Migration in Hybrid Perovskite Solar Cells with Minimal Hysteresis. *Nat. Commun.* **2016**, *7* (1), 13831. https://doi.org/10.1038/ncomms13831.

(12) Jacobs, D. A.; Shen, H.; Pfeffer, F.; Peng, J.; White, T. P.; Beck, F. J.; Catchpole, K. R. The Two Faces of Capacitance: New Interpretations for Electrical Impedance Measurements of Perovskite Solar Cells and Their Relation to Hysteresis. *J. Appl. Phys.* **2018**, *124* (22), 225702. https://doi.org/10.1063/1.5063259.

(13) van Reenen, S.; Kemerink, M.; Snaith, H. J. Modeling Anomalous Hysteresis in Perovskite Solar Cells. *J. Phys. Chem. Lett.* **2015**, *6* (19), 3808–3814. https://doi.org/10.1021/acs.jpclett.5b01645.

(14) Walter, D.; Fell, A.; Wu, Y.; Duong, T.; Barugkin, C.; Wu, N.; White, T.; Weber, K. Transient Photovoltage in Perovskite Solar Cells: Interaction of Trap-Mediated Recombination and Migration of Multiple Ionic Species. *J. Phys. Chem. C* **2018**, *122* (21), 11270–11281. https://doi.org/10.1021/acs.jpcc.8b02529.

(15) Momblona, C.; Gil-Escrig, L.; Bandiello, E.; Hutter, E. M.; Sessolo, M.; Lederer, K.; Blochwitz-Nimoth, J.; Bolink, H. J. Efficient Vacuum Deposited P-i-n and n-i-p Perovskite Solar Cells Employing Doped Charge Transport Layers. *Energy Environ. Sci.* **2016**, *9* (11), 3456–3463. https://doi.org/10.1039/C6EE02100J.

(16) Neukom, M. T.; Züfle, S.; Knapp, E.; Makha, M.; Hany, R.; Ruhstaller, B. Why Perovskite Solar Cells with High Efficiency Show Small IV-Curve Hysteresis. *Sol. Energy Mater. Sol. Cells* **2017**, *169*, 159–166. https://doi.org/10.1016/j.solmat.2017.05.021.